Coupled local residual shear and compressive strain in NaNbO3 ceramics under cooling

Leonardo Oliveira, Mao-Hua Zhang, Marion Höfling, Raquel Rodriguez-Lamas, Can Yildirim, Jurij Koruza, Hugh Simons

Acta Materialia 266 (2024) 119640

Contents lists available at ScienceDirect

Acta Materialia

journal homepage: www.elsevier.com/locate/actamat

Full length article

Coupled local residual shear and compressive strain in $NaNbO_3$ ceramics under cooling

Leonardo Oliveira [a,*], Mao-Hua Zhang [b,c], Marion Höfling [a], Raquel Rodriguez-Lamas [d], Can Yildirim [d], Jurij Koruza [e], Hugh Simons [a,*]

[a] Department of Physics, Technical University of Denmark, 2800 Kgs. Lyngby, Denmark
[b] Department of Materials Science and Engineering, The Pennsylvania State University, University Park, PA 16802, USA
[c] Department of Materials and Earth Sciences, Technical University of Darmstadt, Darmstadt 64287, Germany
[d] European Synchrotron Radiation Facility - ESRF, 71 Avenue des Martyrs, CS40220, 38043 Grenoble Cedex 9, France
[e] Institute for Chemistry and Technology of Materials, Graz University of Technology, Stremayrgasse 9, Graz 8010, Austria

ARTICLE INFO

Keywords:
Antiferroelectrics
Phase transitions
$NaNbO_3$
Shear-strain coupling
Dark-field X-ray microscopy

ABSTRACT

Stabilizing lead-free antiferroelectrics at room temperature is key for advancing greener and more efficient energy storage devices. While $NaNbO_3$ solid solutions hold great promise for high energy density applications, its pure form displays structural instabilities arising from irreversible electric-field induced phase transitions and/or an undesired coexistence with its ferroelectric polymorph. To unravel how mechanical constraints imposed by residual stresses, structural defects, and microstructure disrupt the stability of the $NaNbO_3$ antiferroelectric state, we used *in situ* Dark-Field X-ray Microscopy to map local microstructural deformations in a single embedded $\{100\}_{pc}$ grain. By replicating typical heat treatment conditions, we show that the ferroelectric phase nucleates as a result of the coupled interplay between residual shear and compressive strain distributions that manifest during cooling towards ambient temperature. In addition, the microstrain relaxation behavior indicates that long-range defects preferentially nucleate at the expense of the antiferroelectric phase in regions at *sub*-micrometer distances from the grain center. Our findings illustrate that adequate temperature control during low temperature sintering, heat treatments, or *in operando* conditions may be vital in dictating the structure-property relationships of $NaNbO_3$ ceramics, ensuring their suitability for efficient energy storage applications.

1. Introduction

The electric-field induced transition from the antiferroelectric to the ferroelectric state is fundamental for engineering new energy storage materials. The fingerprint of this transition is typically the presence of a double polarization hysteresis loop, accompanied by large electrostrain, abrupt change of the dielectric constant, and low dielectric loss [1]. Manipulating and controlling these characteristics to yield high recoverable energy density and lower hysteresis is therefore attractive for the development of capacitors with efficient energy storage performance. To this end, specific compositions of $(Pb,La)(Zr,Ti)O_3$-*based* (PLZT) antiferroelectric capacitor materials have shown great promise [2,3]. However, one of the current key challenges in the field is to broaden the range of available lead-free antiferroelectric compositions, while simultaneously achieving comparable performance to PLZT solid solutions.

In the last decade, the development of $NaNbO_3$-*based* materials has sought to realize cost-effective and environmental-friendly antiferroelectrics [4,5]. While many of these chemically-modified $NaNbO_3$ materials exhibit close to zero remanent polarization and well-defined double polarization hysteresis loops at ambient conditions [6–8], the behavior of pure $NaNbO_3$ remains puzzling. For example, while $NaNbO_3$ single crystals show double hysteresis loops along the orthorhombic *c*-axis (*i.e.*, perpendicular to $[001]_{pc}$) and the *pseudocubic* (*pc*) $[111]_{pc}$ direction [9,10], their polycrystals behave differently [11]. In this case, high-energy X-ray diffraction revealed that the quarter-order superstructure reflections of the antiferroelectric *P* phase (*Pbma*) are limited within the first quarter of the hysteresis loop, and then give way to half-order reflections for the subsequent poling cycle [12]. Therefore, an irreversible transformation into the ferroelectric *Q* phase ($P2_1ma$) takes place, limiting its recoverable energy density during discharge due to the high remanent polarization associated with the ferroelectric state.

* Corresponding authors.
E-mail addresses: leosdo@dtu.dk (L. Oliveira), husimo@fysik.dtu.dk (H. Simons).

https://doi.org/10.1016/j.actamat.2023.119640
Received 27 September 2023; Received in revised form 7 December 2023; Accepted 27 December 2023
Available online 28 December 2023

From the atomistic viewpoint, it is known that the local structural distortion between the *P* and *Q* phase is favored under applied electric-fields due to the small relative energies between them [13]. This, in turn, indicates that phase coexistence is preferred, as experimentally observed in a number of experiments [14–18]. However, such calculations do not consider that polycrystals are composed of hierarchical structures of domains, grains, and boundaries that interact with one another during the electric-field- and/or temperature-induced phase transition. Therefore, exploring its microstructural dynamics may clarify the reasons for the limited reversibility of the phase transition, failure mechanisms, and identify new means to stabilize the *P* phase at room temperature.

Another key consideration is that the $NaNbO_3$ perovskite structure possesses a non-trivial sequence of at least five temperature-induced phase transitions, from the high temperature *Pm*-3*m* paraelectric phase to the room temperature *P* or *Q* polymorphs [19–21], due to dynamical phonon mode instabilities mediated by successive NbO_6 octahedral distortions [13]. Furthermore, this complex phase equilibria may influence the nucleation, stabilization, and the critical electric-fields of the antiferroelectric phase, as the variation of the lattice parameters, growth directions, and the number of ferroelastic twin variants – *i.e.,* symmetry reduction without change in Z (the number of atoms of per unit cell) – and antiphase boundaries (symmetry reduction followed by change in Z) plays a role in the relaxation of residual stresses upon cooling. Therefore, probing the evolution of local microstructural features is key to understanding heterogeneity [22], the influence of grain sizes [23,24], the role of structural defects [25], and how phase coexistence can be avoided [14] in the target applications of these materials.

To address the open questions related to the temperature-dependent microstructural evolution of $NaNbO_3$, we investigate their structure-property relationship using *in situ* Dark-field X-ray Microcopy (DFXM). The use of DFXM is advantageous for probing deeply embedded hierarchical structures within the material's bulk. Moreover, this technique offers high spatial and strain resolution, in a non-destructive manner, while preserving the realistic electromechanical boundary conditions representative of macroscopic devices [26,27]. Our results address the interplay between crystal structure, lattice strain, lattice tilt, microstrain, and grain morphologies in a representative $\{100\}_{pc}$ grain of $NaNbO_3$ during *in situ* cooling from the high temperature cubic phase towards the room temperature phases.

2. Experimental procedures

2.1. Sample preparation

$NaNbO_3$ ceramic samples were prepared by the conventional solid-state reaction method using high-purity Na_2CO_3 (99.95 %, Alfa Aesar, Germany) and orthorhombic Nb_2O_5 (99.50 %, Sinopharm, China) dried at 200 °C for 8 h before being weighed at a stoichiometric ratio with 1 wt.% excess Na_2CO_3 to compensate for possible Na evaporation. After ball milling, the powder mixtures were calcined at 850 °C for 4 h, then again subjected to ball milling before sintering. The green pellets were isostatically cold pressed at 200 MPa and sintered at 1355 °C for 3.5 h with a packing powder of the same composition. Polished ceramic pellets with a thickness of 250 μm were prepared for the *in situ* experiment. Further experimental details are found in Ref. [11].

2.2. In situ Dark-field X-ray microscopy

In situ DFXM images were collected at the ID06-HXM beamline of the European Synchrotron Radiation Facility (ESRF), using a photon energy of 16 keV (0.7749 Å). The wavelength and sample size were selected to ensure a safe distance from the Nb absorption edge (19 keV) and at least 20% of beam transmission (as optimized using to *DF-XRM_vis* suite [28]). DFXM images are obtained by positioning an X-ray objective lens along the scattered X-rays of a selected peak within the reciprocal space. The resulting image is a magnified real-space region of a selected *hkl* reflection, with a particular orientation, where the contrast arises from local variations in symmetry and orientation. The X-ray objective consisted of 88 2D Be lenslets and was positioned 234 mm downstream from the sample, which yielded a magnification of 20.35× and effective pixel size of 79 nm.

Herein, we mapped axial strain, lattice tilts, microstrain, and local high resolution Reciprocal Space Maps (RSMs) centered around the $\{100\}_{pc}$ reflection. The spatial variation of the *d*-spacings around $\vec{Q}_{100}$ was scanned by a coupled motion of the X-ray objective lens around 2θ and translation of the far-field detector. Individual ϕ, 2θ, and FWHM maps were decoupled *pixel-by-pixel* using the Gaussian moments approach employed in the *darfix* library [29].

To ensure homogeneous temperature control across the whole sample, the *in situ* isothermal heating measurements were carried out using a bespoke non-contact radiation (optical) furnace for the ID06 beamline, as described in [30]. Prior to the DFXM scans, the sample was heated (at 0.111 W/s ~ 20 K/s, increasing 10 W per step up to 180 W) until the presence of a single peak (characteristic of the high temperature cubic phase) was detected in the RSM. Then, isothermal DFXM scans were taken by slowly cooling down the sample to room temperature (at cooling rate of 0.005 W/s ~ 1 K/s down to 65 W, and then 0.055 W/s ~ 10 K/s down to 0 W).

As further detailed in the RSM section, the impossibility of direct (*i.e.*, contact) temperature measurements at the sample meant that we qualitatively assigned the furnace power to the $NaNbO_3$ phase transitions by comparison of the limiting onset and offset *d*-spacings of published crystallographic data in [20,31–33]. This approach is suitable for a qualitative phase indexation at each applied furnace power (see Table 1 for a detailed power-phase relationship), specifically to differentiate the orthorhombic-to-orthorhombic transitions present in $NaNbO_3$.

3. Results and discussion

3.1. Qualitative indexing of in situ $NaNbO_3$ phase transitions from local RSMs

Fig. 1 shows the local RSMs measured from a single embedded $NaNbO_3$ grain, at different power intervals upon cooling, and depicts how the phases evolve from room temperature towards the high-symmetry cubic phase. The successive peak splitting from 180 W to 0 W in both 2θ and η (detector azimuthal angle) reveals that several phase transitions take place, as well as a variation in the number of ferroelastic twin variants, respectively. At 180 W, the RSM displays a single peak, denoting that the last polymorphic phase (the paraelectric cubic state) was reached.

Using the method described in Section 2.2 to qualitatively index the phase transitions, Fig. 2a displays the evolution of the peak splitting integrated over 2θ. The first phase transition is identified above 85 W, where the previously well-defined Bragg peaks are merged, followed by a change in the relative intensity between them. Despite the fact that most of the phases below 592 °C exhibit orthorhombic symmetry, the long sample-to-detector distance (~ 5 m) allows us to identify additional splitting (in the order of 0.003°) that is not usually seen in regular synchrotron XRD. This approach provides additional insight into the

Table 1
Simplified phase labelling used in this work, according to their indexed phase at specific applied finance power prior to DFXM scans.

Power (W)	180	170	135	130	115	65	0
Label	U180	$T_2$170	S135	S130	R115	P65	Q0
Space group	*Pm-3m*	*P4/mbm*	*Pbnm*		*Pbnm*	*Pbma*	$P2_1ma$
Z	1	2	24		12	8	4

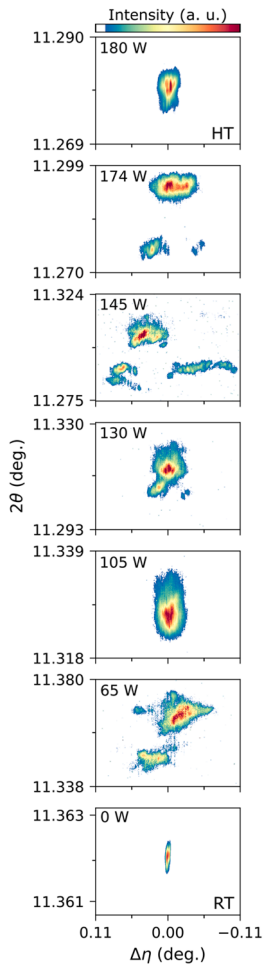

Fig. 1. High-resolution local RSMs on $\{100\}_{pc}$ grain at selected applied furnace powers upon cooling: from the high temperature (HT) phase at 180 W towards the room temperature (RT) state at 0 W. Note that the final measurement (0 W) likely exhibits strong splitting that was not captured by the limited angular range of the final RSM measurement.

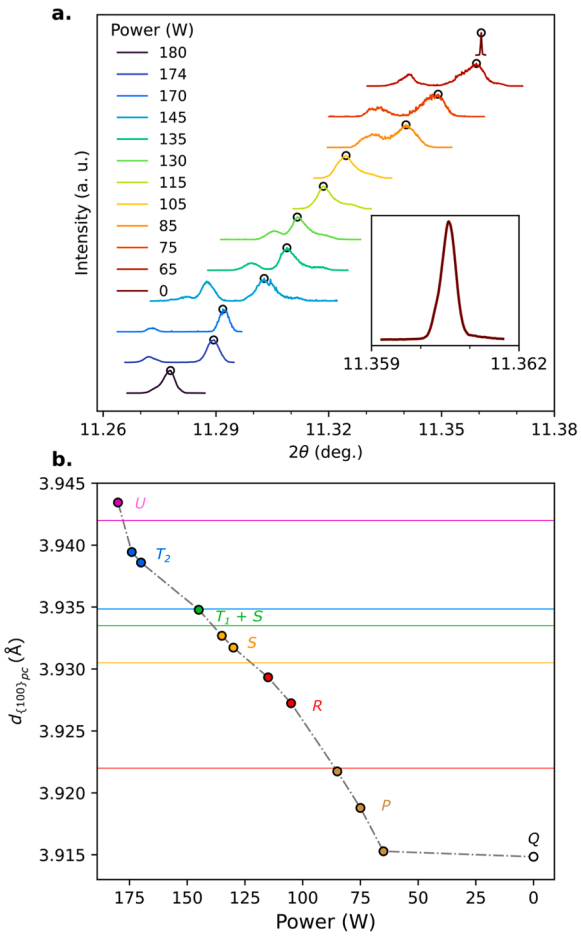

Fig. 2. Furnace power-dependent (a) RSMs integrated over 2θ for $\{100\}_{pc}$ reflection. The insert in (a) highlights only the right-most intense peak at 0 W in a smaller region in the reciprocal space. The position of circle markers at the rightmost intense 2θ peak in (a) is plotted in (b) and as a function of the *d*-spacing *vs.* power to track the evolution of the phase transitions. The horizontal lines in (b) represent the expected onset and offset of the $\{100\}_{pc}$ *d*-spacing for each of the $NaNbO_3$ phases observed, as detailed in section 2.2. The transition line between *P* to *Q*, which is often seen as driven by electric fields, is missing.

phase identification in individual grains, particularly in distinguishing mixed phase regions and the sequence of orthorhombic phase transitions in $NaNbO_3$.

According to the expected *d*-spacings for each phase based on the $\{100\}_{pc}$ reflections selected in Fig. 2a, the horizontal lines in Fig. 2b identifies seven $NaNbO_3$ phases in the range between 180 W and 0 W. A possible phase coexistence is present at 145 W, considering that the splitting into four peaks does not represent either the T_1 or S phase individually (*i.e.*, the T_1-phase is expected to split into $(0\ 2\ 2)_o$, $(2\ 0\ 2)_o$, and $(2\ 2\ 0)_o$, while the S-phase would split into the $(1\ 1\ 12)_o$ and $(2\ 0\ 0)_o$ peaks, where the subscript "o" denotes orthorhombic notation). Rather, the low angle reflections are likely due to the formation of T_1 domains (this coexistence used to be called *W* phase after [34]). As previously mentioned, it is important to stress that *P* and *Q* phase coexistence has been widely reported at room temperature. However, considering that both room temperature orthorhombic polymorphs obey almost the same systematic absence rules, (*i.e.,* the fundamental reflections of both phases match at the same Bragg angle) conclusive phase identification is challenging when only indexing the splitting of the $\{100\}_{pc}$ peak.

Therefore, here we substantiate our argument supported by DFXM that the room temperature *P* and *Q* polymorphs exert distinct contributions on lattice strain, lattice tilt, and microstrain maps. These maps strongly suggest that the phase observed at 0 W is a *Q* phase or a mixture where their volume is substantial enough to induce such alterations.

Subsequently, the sample for each applied furnace power is simply labeled according to Table 1.

3.2. Evolution of residual lattice strain, lattice tilt, and microstrain in a single embedded grain

A typical DFXM strain map resolves the residual stress-strain state distribution within a microstructure, including their intergranular features. In Eqs. (1)–(3) we define the relative *i*) intrinsic lattice strain (ε_r^E), *ii*) microstrain (ε_r^M), and *iii*) lattice tilt ($Tilt_r$) parameters used to quantify the influence of strain and shear stresses. While the ε_r^E considers only uniform changes in *d*-spacing of the coherent diffracting domains, the ε_r^M is affected by non-uniform structural distortions due to microstructural inhomogeneities at *sub*-pixel length scales (< 100 nm) caused by the presence of structural defects. Meanwhile, $Tilt_r$ is commonly associated with the effect of shear stresses in the lattice.

$$\varepsilon_r^E = 100 \times \left(\frac{\sin\bar{\theta}}{\sin\theta} - 1\right) \tag{1}$$

$$\varepsilon_r^M = \varepsilon^M - \overline{\varepsilon^M} \tag{2}$$

$$Tilt_r = Tilt - \overline{Tilt} \tag{3}$$

where $\overline{\theta}$, $\overline{\varepsilon^M}$, and $\overline{Tilt}$ correspond to the average value at each furnace power applied, being $\varepsilon^M = FWHM_\theta/4 \times \tan\theta$, and $Tilt = \phi - \theta$.

The relative lattice strain maps in Fig. 3a display a heterogenous distribution across several phase transitions in an embedded grain. We observed that positive (tensile) and negative (compressive) deviations from the mean strain values tend to be redistributed along the periphery of the grain boundaries as the sample cools down. This implies that the stain states are highly dependent on the grain interactions with its surroundings (*i.e.*, an extrinsic phenomena), given that the bulk modulus (*e.g.*, 158 GPa [35]) is not expected to present significant variations among polymorphs. Apart from the conditions close to the room temperature phase, *e.g.,* at P65 and *Q*0, the effect of cooling down the sample shows a preferred relaxation towards the grain centers, with ε_r^E close to zero.

The residual ε_r^E distribution between the *R* to *P* and *P* to *Q* orthorhombic phases shows a distinct behavior not observed in the other high temperature phases. From R115 towards room temperature, traces of residual strains shift towards the grain centers. This change in strain heterogeneity is a complex mechanical phenomena, most likely related to *i*) the intrinsic anisotropic mechanical and thermal properties, *ii*) extrinsic anisotropic local environment (*i.e.,* meeting of grains with different orientations, exacerbated by $NaNbO_3$'s unusually strong anisotropy in thermal expansion), and *iii*) stress-dependent phase transitions, which are strongly influenced by the first-order nature of the structural phase transition between the AFE-to-AFE states (between *R* and *P* phases), and the AFE-to-FE states (between *P* to *Q* phases). At the same time, we also note an apparent reduction in the measured grain diameter: from 6.19 μm in R115 to 5.96 μm in P65, and then to 3.69 μm in *Q*0. This is not a reduction in grain size, but a measurement artefact due to increased structural disorder at the grain periphery (*i.e.,* wider scattering angles that fall beyond the numerical aperture and scanning range of the X-ray objective lens).

At the same time, the $Tilt_r$ maps shown in Fig. 3b depict a very similar behavior observed in the ε_r^E maps, especially in regions where the high strains and tilt are locally accumulated. Again, the most significant changes are observed across the *R* to *P* phase transition and between the room temperature *P* and *Q* states. Fig. 4a,b reveals that, whereas the spread in ε_r^E remains almost constant above R115, in $Tilt_r$ it increases, splits, and shows a local minimum centered in zero. This indicates that shear stresses hold considerable importance and may play a significant role in the phase transition and, consequently, in the relaxation of residual shear and strain in the room temperature antiferroelectric phase after cooling. In this sense, the reconstructed maps shown in Fig. 3 for *Q*0 are distinct from the high temperature phases and display a new relaxation mechanism that preserves ε_r^E close to zero at the grain center of mass at the expense of negative $Tilt_r$ in this region.

In the same way, the distributions shown in Fig. 4a,b for *Q*0 are now broader and delocalized. Interestingly, *Q*0 presents a new $Tilt_r$ mode close to 0.25 %, which may be coupled to ε_r^E, displaying a new intense compressive strain mode close to -0.5 %. This additional compressive strain will then result in *i*) a distribution of uncompensated nano domain structures with a high density of defects, and/or *ii*) shear-induced nucleation of the ferroelectric *Q* phase. While the former can potentially lead to lower breakdown strength and failure under applied electric-field due to large volumetric change the structure must withstand (a value of ~ 0.60 % in the longitudinal direction), the latter may promote an irreversible transition to a phase that compromises the double hysteresis loop behavior of polarization and, consequently, the energy storage density of the material.

Fig. 3c shows that the influence of the microstrain, ε_r^M, is minimal for each measured phase, with the most intense contribution found in U180 due to the more disordered structure at the grain boundaries. In addition, the structural heterogeneities display a systematic variation for each temperature/power measured, with a continuous decay from the high values located at the grain boundaries, to the lower ones at the grain center of mass. This observation agrees with the expectations for polycrystalline ceramics, including polycrystalline ferroelectrics [36–38]. Therefore, the distortion field caused by crystalline defects is concentrated in a *sub*micron-sized region across the grain boundary. Moreover, its distribution shown in Fig. 4c follows a logarithmic-*like* decay, with the most significant variation observed at the *Q*0, along with a slight shift towards negative relative values as the grain transforms its shape.

3.3. Average spatial variation of the relaxation mechanisms across phase transitions

In order to obtain a more quantitative description about the material behavior associated with distinct regions of the grain, we introduce a methodology consisting of obtaining the microstrain and elastic energy distribution for pixels that are equidistant from the grain boundary using Euclidean distance transformation (implemented as *distance_transform_edt* in *Scipy* [39]). From the contours shown in Fig. 5, we obtain the average values of strain, microstrain, and elastic energy for each position along the whole grain.

Following the elasticity theory, Krivoglaz [40] classified structural defects according to the rate of displacements at large distances from those defects according to Eq. (4). Herein, *r* is the distance from the grain

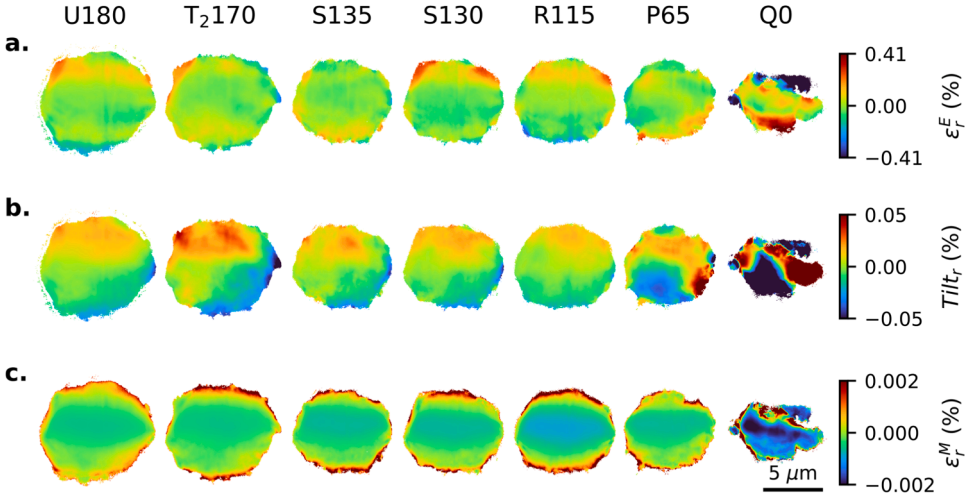

Fig. 3. Reconstructed DFXM maps of relative (a) strain, (b) lattice tilt, and (c) microstrain for cooling down $NaNbO_3$ from the paraelectric cubic U180 phase towards the room temperature ferroelectric *Q*0 phase.

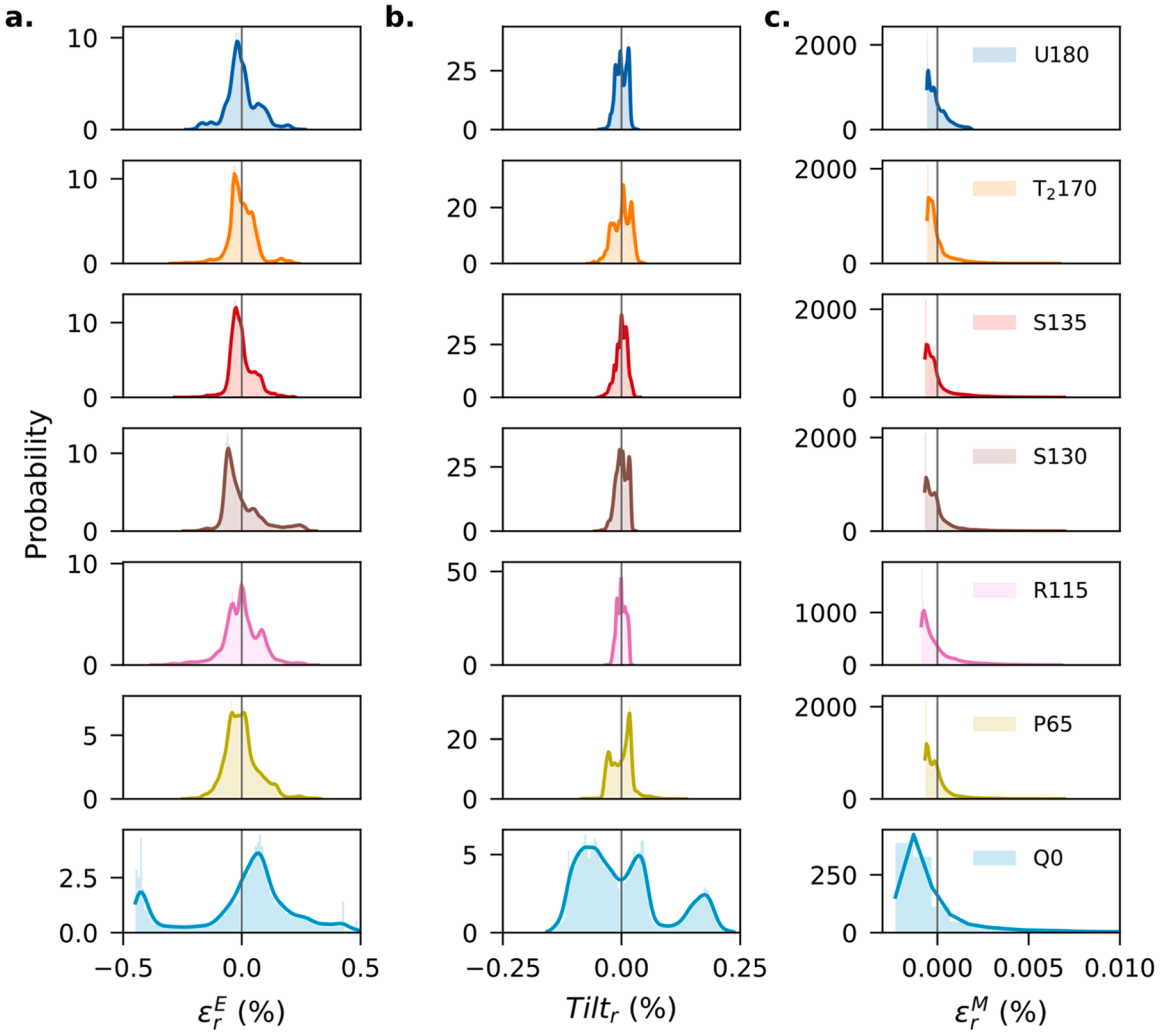

Fig. 4. Histograms of relative (a) lattice strain, (b) lattice tilt, and (c) microstrain for $NaNbO_3$, covering all *in situ* DFXM measurements under different applied furnace power conditions. The solid lines correspond to the probability density function fitting.

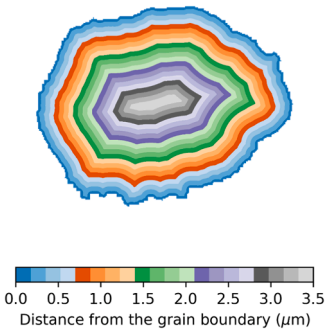

Fig. 5. Example of distance to grain boundary calculation. The unique values of elastic strain and microstrain at a specific position are spatially averaged of all equidistant distances (or layers) relative to the grain boundary.

boundary to the grain center, and B is the relaxation constant. In general, short-range defects decay as r^{-2} (or at higher rates), while the long-range ones decay as $r^{-3/2}$ (or at slower rates) [41,42]. Fig. 6a (axis inverted for clarity) shows that the defects are highly localized at the grain boundaries, following a decay expected for long-range defects according to fitted relaxations constants. Therefore, it means the observed microstrain broadening is dominated by long-range defects, and not by short-range defects, such as point defects.

$$\varepsilon_r^M \sim r^{-B} \tag{4}$$

Although the microstrain maps show similar distribution across several phase transitions, significant changes are present between the P65 to *Q*0 transition. Specifically, P65 displays a faster relaxation decay in contrast to *Q*0 and R115, most likely related to the additional formation of twins (*e.g.*, to release mechanical incompatibilities raised by non-quasi-static cooling) and/or antiphase boundaries (common long-range planar defects observed in $NaNbO_3$ [25]). At these stages, anomalies from the expected decay are evident at 1.12 μm and 1.63 μm, respectively. To consider these humps in the fitting model, we modified the Eq. (4) to include a gaussian distribution in addition to the exponential decay, as shown in Eq. (5)

$$\varepsilon_r^M \sim r^{-B} + \frac{1}{\sigma\sqrt{2\pi}}\exp\left[-\frac{1}{2}\left(\frac{r-\mu}{\sigma}\right)^2\right] \tag{5}$$

where μ and σ are the gaussian peak center and width, respectively.

The unexpected appearance of a distinct anomalous hump in the microstrain relaxation of *Q*0 is a significant deviation from the Krivoglaz formalism for microstrain relaxation from defects. While it has been established that the introduction of precipitates of a new phase does not lead to significant broadening of the Bragg peaks, this may not be the case given the complex morphologies regularly seen in pure $NaNbO_3$.

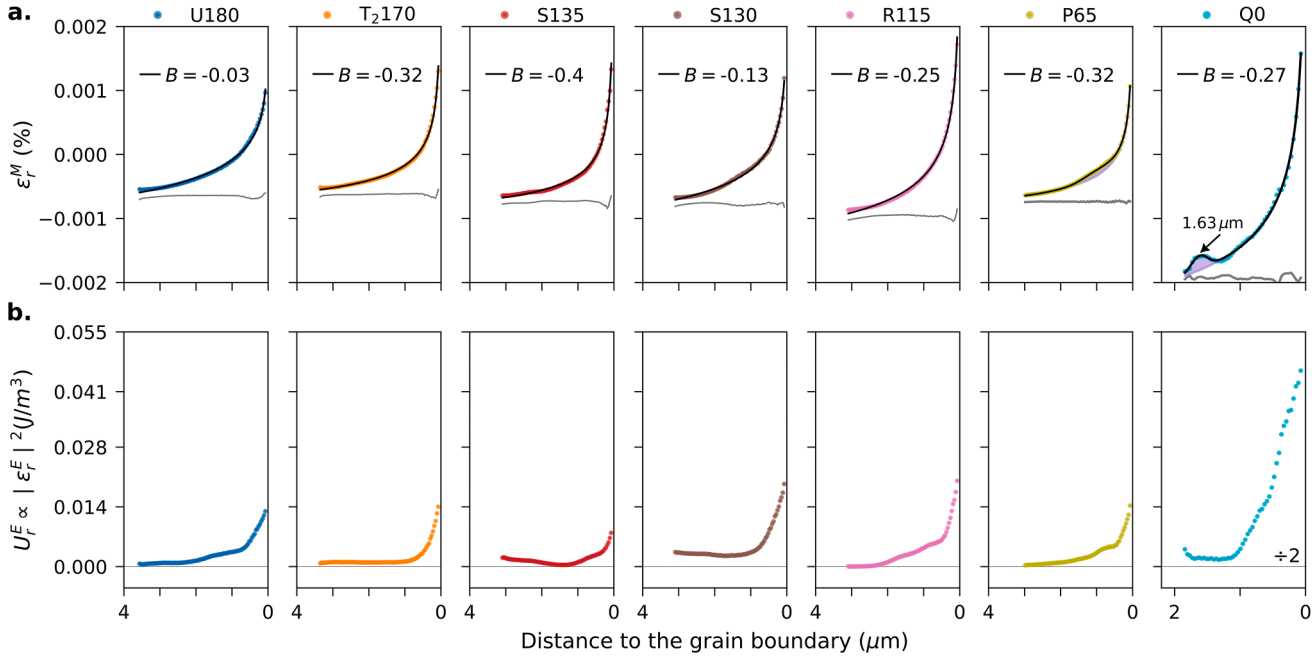

Fig. 6. (a) Relative microstrain and (b) elastic energy relaxation towards the grain center. The solid black lines in (a) correspond to the fitting from Eqs. (4) and (5), whereas the light gray ones represent the residuals. All the fitted curves display R^2 greater than 0.97. Shaded areas highlight regions where the gaussian anomaly is evident. The anomalous peak in *Q*0 is centered at 1.63 μm, with width of 126 nm. To facilitate comparison with the high temperature phases, the U_r^E at *Q*0 has been halved.

Guo et al. have shown that individual grains of $NaNbO_3$ exhibits coexistence of AFE and FE phase, alongside hierarchical polydomain morphologies with mixed diffused and well-defined phase boundaries [43]. Furthermore, in Refs. [44,45], there is clear evidence indicating that regions where the *Q* phase is detected are enclosed by the *P* phase. Although there is currently no clear theory of antiphase domain formation and relaxation in $NaNbO_3$, the hump in *Q*0 suggests that, upon cooling, long-range defects are preferentially nucleated close to – but not at – the $\{100\}_{pc}$ grain center. These defects appear to play a significant role in the transformation from the antiferroelectric *P* phase to the metastable ferroelectric *Q* phase.

In Fig. 6b, the complex behavior of the relative elastic energy, $U_r^E \propto |\varepsilon_r^E|^2$, across several phase transitions indicates the elastic energy experiences an exponential-*like* decay from the defect rich grain boundaries towards the grain centers. Deviations from the expected asymptotic behavior appear as multiple decay steps and are likely related to relative strain-free regions separating ferroelastic twin boundaries to minimize the energy associated to regions with distinct misorientations and density of defects. Therefore, these boundaries occur due to the inhomogeneous ε_r^E distribution, and the anisotropic environment where the grain is clamped. At the same time, they also act as a source of internal stress, helping the grain to keep its shape (as seen from U180 to P65 in Fig. 3) [46].

It is important to stress that cooling rate may have a significant influence on the residual stress gradients, aiding the room temperature nucleation of the non-ideal ferroelectric *Q* phase for energy storage applications. Considering the tensorial properties of the phase transitions, the nucleation of the antiferroelectric phase is favored when the full ferroelastic transition between the cubic to the room temperature orthorhombic $m\bar{3}m - m_{xy}m_{\bar{x}y}m_z$ species (*i.e.,* *U* to *P* phase transition) takes place (six distinct non-degenerated orientational ferroelastic domain states). This transformation seems to be the case when slow cooling rates are applied during the sintering process, and/or when the pure $NaNbO_3$ displays large grain sizes.

On the other hand, the nucleation of ferroelectric *Q* phase is preferred when the transition from the cubic prototype to less symmetrical orthorhombic $m\bar{3}m - m_{xy}m_{\bar{x}y}2_z$ species takes place. In this transformation, a coupling of polarization and strain gives place to six double-degenerated ferroelastic and ferroelectric domains. At the same time, it develops a non-zero polarization along the [0 0 1] axis, with the thermal dilatation tensor revealing a spontaneous, symmetry-breaking shear deformation along ε_{xy} that favors the ferroelectric phase *Q* to form [47]. Previous studies on strain-induced phase transition by epitaxial growth of $NaNbO_3$ thin films have demonstrated that the formation of ferroelectric phases is preferred under compressive strain at room temperature [48,49]. However, the observation of the compressive strain and shear strain coupling on inducing an antiferroelectric to ferroelectric phase transition by cooling, to the best of our knowledge, has not been discussed.

4. Conclusions

In summary, *in situ* Dark-field X-ray Microscopy in $NaNbO_3$ ceramics revealed, for the first time, that the adequate control of local shear stresses is likely critical for the stabilization of the antiferroelectric *P* phase at room temperature. We have shown that controlling the cooling rates, and most likely its thermal gradient, is essential for preventing the occurrence of heterogenous distribution of positive shear stresses peaks, and the consequent distribution of compressive strained states that may induce the nucleation of the ferroelectric *Q* polymorph at room temperature. The observed shear-strain coupling, therefore, provides additional insight into thermal treatments, best practices of low temperature sintering and the adequate temperature control under *in operando* conditions to keep the antiferroelectric phase stable at room temperature. Therefore, our finding presents a novel perspective on the structure-property relationship of $NaNbO_3$, which is expected to impact the shear-strain engineering on the current ceramic processing methods and benefit the development of future $NaNbO_3$-*based* antiferroelectrics with improved energy storage efficiency. This work expands the capabilities of DFXM as a tool to probe phase transitions based on lattice tilt and strain distributions analysis in polycrystals with similar crystallographic systematic absence rules.

Data availability

Data will be made available on request.

Declaration of Competing Interest

The authors declare that they have no known competing financial interests or personal relationships that could have appeared to influence the work reported in this paper.

Acknowledgment

The authors are grateful to ESRF for providing beamtime at ID06-HXM under proposal MA-4442. L.O., M.H., and H.S. acknowledge financial support from ERC Starting Grant #804665. This work was partially supported by the Hessian State Ministry for Higher Education, Research, and the Arts under the LOEWE collaborative project FLAME (Fermi level engineering of antiferroelectric materials for energy storage and insulation systems).

References

[1] C.A. Randall, Z. Fan, I. Reaney, L. Chen, S. Trolier-McKinstry, Antiferroelectrics: history, fundamentals, crystal chemistry, crystal structures, size effects, and applications, J. Am. Ceram. Soc. 104 (2021) 3775–3810, https://doi.org/10.1111/jace.17834.

[2] H. Wang, Y. Liu, T. Yang, S. Zhang, Ultrahigh energy-storage density in antiferroelectric ceramics with field-induced multiphase transitions, Adv. Funct. Mater. 29 (2019) 1807321, https://doi.org/10.1002/adfm.201807321.

[3] G. Ge, C. Shi, C. Chen, Y. Shi, F. Yan, H. Bai, J. Yang, J. Lin, B. Shen, J. Zhai, Tunable domain switching features of incommensurate antiferroelectric ceramics realizing excellent energy storage properties, Adv. Mater. 34 (2022) 2201333, https://doi.org/10.1002/adma.202201333.

[4] M.H. Zhang, L. Fulanović, C. Zhao, J. Koruza, Review on field-induced phase transitions in lead-free $NaNbO_3$-based antiferroelectric perovskite oxides for energy storage, J. Mater. 9 (2023) 1–18, https://doi.org/10.1016/j.jmat.2022.09.008.

[5] J. Jiang, X. Li, L. Li, S. Guo, J. Zhang, J. Wang, H. Zhu, Y. Wang, S.T. Zhang, Novel lead-free $NaNbO_3$-based relaxor antiferroelectric ceramics with ultrahigh energy storage density and high efficiency, J. Mater. 8 (2022) 295–301, https://doi.org/10.1016/j.jmat.2021.09.007.

[6] M.H. Zhang, H. Ding, S. Egert, C. Zhao, L. Villa, L. Fulanović, P.B. Groszewicz, G. Buntkowsky, H.J. Kleebe, K. Albe, A. Klein, J. Koruza, Tailoring high-energy storage $NaNbO_3$-based materials from antiferroelectric to relaxor states, Nat. Commun. 14 (2023) 1525, https://doi.org/10.1038/s41467-023-37060-4.

[7] Z. Chen, S. Mao, L. Ma, G. Luo, Q. Feng, Z. Cen, F. Toyohisa, X. Peng, L. Liu, H. Zhou, C. Hu, N. Luo, Phase engineering in $NaNbO_3$ antiferroelectrics for high energy storage density, J. Mater. 8 (2022) 753–762, https://doi.org/10.1016/j.jmat.2022.03.004.

[8] N. Luo, L. Ma, G. Luo, C. Xu, L. Rao, Z. Chen, Z. Cen, Q. Feng, X. Chen, F. Toyohisa, Y. Zhu, J. Hong, J.F. Li, S. Zhang, Well-defined double hysteresis loop in $NaNbO_3$ antiferroelectrics, Nat. Commun. 14 (2023) 1776, https://doi.org/10.1038/s41467-023-37469-x.

[9] L.E. Cross, B.J. Nicholson, The optical and electrical properties of single crystals of sodium niobate, Lond. Edinb. Dublin Philos. Mag. J. Sci. 46 (1955) 453–466, https://doi.org/10.1080/14786440508520582.

[10] D. Yang, Y. Zhang, X. Wang, Q. Li, J. Li, Antiferroelectricity of $NaNbO_3$: single-crystal experimental study and first-principles calculation, J. Am. Ceram. Soc. 105 (2022) 5555–5561, https://doi.org/10.1111/jace.18526.

[11] M.H. Zhang, L. Fulanović, S. Egert, H. Ding, P.B. Groszewicz, H.J. Kleebe, L. Molina-Luna, J. Koruza, Electric-field-induced antiferroelectric to ferroelectric phase transition in polycrystalline $NaNbO_3$, Acta Mater. 200 (2020) 127–135, https://doi.org/10.1016/j.actamat.2020.09.002.

[12] M.H. Zhang, C. Zhao, L. Fulanović, J. Rödel, N. Novak, A. Schökel, J. Koruza, Revealing the mechanism of electric-field-induced phase transition in antiferroelectric $NaNbO_3$ by *in situ* high-energy x-ray diffraction, Appl. Phys. Lett. 118 (2021) 132903, https://doi.org/10.1063/5.0043050.

[13] K. Kim, W. Hwang, J.H. Lee, A. Soon, Explicating the irreversible electric-field-assisted ferroelectric phase transition in the otherwise antiferroelectric sodium niobate for energy storage systems, J. Mater. Chem. C 10 (2022) 10500–10510, https://doi.org/10.1039/D2TC01817A.

[14] L.A. Reznichenko, L.A. Shilkina, E.S. Gagarina, I.P. Raevskii, E.A. Dul'kin, E. M. Kuznetsova, V.V. Akhnazarova, Structural instabilities, incommensurate modulations and P and Q phases in sodium niobate in the temperature range 300–500K, Crystallogr. Rep. 48 (2003) 448–456, https://doi.org/10.1134/1.1578130.

[15] I. Lefkowitz, K. Łukaszewicz, H.D. Megaw, The high-temperature phases of sodium niobate and the nature of transitions in pseudosymmetric structures, Acta Cryst. 20 (1966) 670–683, https://doi.org/10.1107/S0365110x66001592.

[16] H. Shimizu, H. Guo, S.E. Reyes-Lillo, Y. Mizuno, K.M. Rabe, C.A. Randall, Lead-free antiferroelectric: $xCaZrO_3$ -(1 −x)</number>$NaNbO_3$ system ($0 \leq x \leq 0.10$), Dalton Trans. 44 (2015) 10763–10772, https://doi.org/10.1039/C4DT03919J.

[17] R.A. Shakhovoy, S.I. Raevskaya, L.A. Shakhovaya, D.V. Suzdalev, I.P. Raevski, Yu. I. Yuzyuk, A.F. Semenchev, M. El Marssi, Ferroelectric Q and antiferroelectric P phases' coexistence and local phase transitions in oxygen-deficient $NaNbO_3$ single crystal: micro-Raman, dielectric and dilatometric studies: ferroelectric Q and antiferroelectric P phases' coexistence, J. Raman Spectrosc. 43 (2012) 1141–1145, https://doi.org/10.1002/jrs.3140.

[18] W. Li, X. Xia, J. Zeng, L. Zheng, G. Li, Significant differences in $NaNbO_3$ ceramics fabricated using Nb_2O_5 precursors with various crystal structures, Ceram. Int. 46 (2020) 3759–3766, https://doi.org/10.1016/j.ceramint.2019.10.098.

[19] S.K. Mishra, N. Choudhury, S.L. Chaplot, P.S.R. Krishna, R. Mittal, Competing antiferroelectric and ferroelectric interactions in $NaNbO_3$: neutron diffraction and theoretical studies, Phys. Rev. B 76 (2007) 024110, https://doi.org/10.1103/PhysRevB.76.024110.

[20] S.K. Mishra, R. Mittal, V.Yu. Pomjakushin, S.L. Chaplot, Phase stability and structural temperature dependence in sodium niobate: a high-resolution powder neutron diffraction study, Phys. Rev. B 83 (2011) 134105, https://doi.org/10.1103/PhysRevB.83.134105.

[21] H.D. Megaw, The seven phases of sodium niobate, Ferroelectrics 7 (1974) 87–89, https://doi.org/10.1080/00150197408237956.

[22] J. Ormstrup, E.V. Østergaard, M.S. Christensen, C. Yildirim, P.K. Cook, M. Kutsal, T. Olsen, H. Simons, Bulk heterogeneity in barium titanate above the Curie temperature, Appl. Phys. Lett. 119 (2021) 202901, https://doi.org/10.1063/5.0065834.

[23] J. Koruza, P. Groszewicz, H. Breitzke, G. Buntkowsky, T. Rojac, B. Malič, Grain-size-induced ferroelectricity in $NaNbO_3$, Acta Mater. 126 (2017) 77–85, https://doi.org/10.1016/j.actamat.2016.12.049.

[24] Y. Shiratori, A. Magrez, J. Dornseiffer, F.H. Haegel, C. Pithan, R. Waser, Polymorphism in micro-, submicro-, and nanocrystalline $NaNbO_3$, J. Phys. Chem. B 109 (2005) 20122–20130, https://doi.org/10.1021/jp052974p.

[25] H. Ding, M. Zhang, J. Koruza, L. Molina-Luna, H. Kleebe, Domain morphology of newly designed lead-free antiferroelectric $NaNbO_3$ -$SrSnO_3$ ceramics, J. Am. Ceram. Soc. 104 (2021) 3715–3725, https://doi.org/10.1111/jace.17738.

[26] H. Simons, A.B. Haugen, A.C. Jakobsen, S. Schmidt, F. Stöhr, M. Majkut, C. Detlefs, J.E. Daniels, D. Damjanovic, H.F. Poulsen, Long-range symmetry breaking in embedded ferroelectrics, Nat. Mater. 17 (2018) 814–819, https://doi.org/10.1038/s41563-018-0116-3.

[27] H. Simons, A. King, W. Ludwig, C. Detlefs, W. Pantleon, S. Schmidt, F. Stöhr, I. Snigireva, A. Snigirev, H.F. Poulsen, Dark-field X-ray microscopy for multiscale structural characterization, Nat. Commun. 6 (2015) 6098, https://doi.org/10.1038/ncomms7098.

[28] T.M. Ræder, Dark-field X-ray microscopy visualization, JOSS 8 (2023) 5177, https://doi.org/10.21105/joss.05177.

[29] J. Garriga Ferrer, R. Rodríguez-Lamas, H. Payno, W. De Nolf, P. Cook, V.A. Solé Jover, C. Yildirim, C. Detlefs, *darfix* – data analysis for Dark-field X-ray microscopy, J. Synchrotron Radiat. 30 (2023), https://doi.org/10.1107/S1600577523001674.

[30] C. Yildirim, H. Vitoux, L.E. Dresselhaus-Marais, R. Steinmann, Y. Watier, P. K. Cook, M. Kutsal, C. Detlefs, Radiation furnace for synchrotron Dark-field x-ray microscopy experiments, Rev. Sci. Instrum. 91 (2020) 065109, https://doi.org/10.1063/1.5141139.

[31] R.H. Mitchell, P.C. Burns, K.S. Knight, C.J. Howard, A.R. Chakhmouradian, Observations on the crystal structures of lueshite, Phys. Chem. Miner. 41 (2014) 393–401, https://doi.org/10.1007/s00269-014-0657-1.

[32] R.H. Mitchell, B.J. Kennedy, K.S. Knight, The crystal structure of lueshite at 298K resolved by high-resolution time-of-flight neutron powder diffraction, Phys. Chem. Miner. 45 (2018) 77–83, https://doi.org/10.1007/s00269-017-0905-2.

[33] S.G. Jabarov, D.P. Kozlenko, S.E. Kichanov, A.V. Belushkin, A.I. Mammadov, B. N. Savenko, R.Z. Mekhtieva, C. Lathe, Structural studies of the P-T phase diagram of sodium niobate, J. Synch. Investig. 6 (2012) 546–551, https://doi.org/10.1134/S1027451012060250.

[34] A.M. Glazer, H.D. Megaw, Studies of the lattice parameters and domains in the phase transitions of $NaNbO_3$, Acta Cryst. A 29 (1973) 489–495, https://doi.org/10.1107/S0567739473001245.

[35] S.K. Mishra, M.K. Gupta, R. Mittal, S.L. Chaplot, T. Hansen, Suppression of antiferroelectric state in $NaNbO_3$ at high pressure from *in situ* neutron diffraction, Appl. Phys. Lett. 101 (2012) 242907, https://doi.org/10.1063/1.4771983.

[36] J. Schultheiß, S. Checchia, H. Uršič, T. Frömling, J.E. Daniels, B. Malič, T. Rojac, J. Koruza, Domain wall-grain boundary interactions in polycrystalline Pb(Zr0.7Ti0.3)O3 piezoceramics, J. Eur. Ceram. Soc. 40 (2020) 3965–3973, https://doi.org/10.1016/j.jeurceramsoc.2020.03.054.

[37] J. Schultheiß, L. Porz, L. Kodumudi Venkataraman, M. Höfling, C. Yildirim, P. Cook, C. Detlefs, S. Gorfman, J. Rödel, H. Simons, Quantitative mapping of nanotwin variants in the bulk, Scr. Mater. 199 (2021) 113878, https://doi.org/10.1016/j.scriptamat.2021.113878.

[38] A. Zimmermann, E.R. Fuller, J. Rödel, Residual stress distributions in ceramics, J. Am. Ceram. Soc. 82 (2004) 3155–3160, https://doi.org/10.1111/j.1151-2916.1999.tb02217.x.

[39] C.R. Harris, K.J. Millman, S.J. Van Der Walt, R. Gommers, P. Virtanen, D. Cournapeau, E. Wieser, J. Taylor, S. Berg, N.J. Smith, R. Kern, M. Picus, S. Hoyer, M.H. Van Kerkwijk, M. Brett, A. Haldane, J.F. Del Río, M. Wiebe, P. Peterson, P. Gérard-Marchant, K. Sheppard, T. Reddy, W. Weckesser, H. Abbasi, C. Gohlke, T.E. Oliphant, Array programming with NumPy, Nature 585 (2020) 357–362, https://doi.org/10.1038/s41586-020-2649-2.

[40] M.A. Krivoglaz, V.G. Baryakhtar, M.A. Ivanov, S.C. Moss, J. Peisl, X-Ray and Neutron Diffraction in Nonideal Crystals, Springer Berlin Heidelberg, Berlin, Heidelberg, 1996, https://doi.org/10.1007/978-3-642-74291-0.
[41] A. Stukowski, J. Markmann, J. Weissmüller, K. Albe, Atomistic origin of microstrain broadening in diffraction data of nanocrystalline solids, Acta Mater. 57 (2009) 1648–1654, https://doi.org/10.1016/j.actamat.2008.12.011.
[42] Z. Zhang, É. Ódor, D. Farkas, B. Jóni, G. Ribárik, G. Tichy, S.H. Nandam, J. Ivanisenko, M. Preuss, T. Ungár, Dislocations in grain boundary regions: the origin of heterogeneous microstrains in nanocrystalline materials, Metall. Mater. Trans. A 51 (2020) 513–530, https://doi.org/10.1007/s11661-019-05492-7.
[43] H. Guo, H. Shimizu, Y. Mizuno, C.A. Randall, Domain configuration changes under electric field-induced antiferroelectric-ferroelectric phase transitions in $NaNbO_3$ -based ceramics, J. Appl. Phys. 118 (2015) 054102, https://doi.org/10.1063/1.4928153.
[44] H. Guo, H. Shimizu, Y. Mizuno, C.A. Randall, Strategy for stabilization of the antiferroelectric phase (*Pbma*) over the metastable ferroelectric phase (*P21ma*) to establish double loop hysteresis in lead-free (1− x) $NaNbO_3$- *x* $SrZrO_3$ solid solution, J. Appl. Phys. 117 (2015) 214103, https://doi.org/10.1063/1.4921876.
[45] H. Guo, H. Shimizu, C.A. Randall, Microstructural evolution in $NaNbO_3$-based antiferroelectrics, J. Appl. Phys. 118 (2015) 174107, https://doi.org/10.1063/1.4935273.
[46] G. Arlt, Twinning in ferroelectric and ferroelastic ceramics: stress relief, J. Mater. Sci. 25 (1990) 2655–2666, https://doi.org/10.1007/BF00584864.
[47] A.K. Tagantsev, L.E. Cross, J. Fousek, Domains in Ferroic Crystals and Thin Films, Springer, New York, 2010, https://doi.org/10.1007/978-1-4419-1417-0. New York, NY.
[48] J. Schwarzkopf, M. Schmidbauer, T. Remmele, A. Duk, A. Kwasniewski, S. Bin Anooz, A. Devi, R. Fornari, Strain-induced phase transitions in epitaxial $NaNbO_3$ thin films grown by metal–organic chemical vapour deposition, J. Appl. Crystallogr. 45 (2012) 1015–1023, https://doi.org/10.1107/S0021889812035911.
[49] M. Tyunina, J. Levoska, Unstable state in epitaxial films of sodium niobate, Appl. Phys. Lett. 95 (2009) 102903, https://doi.org/10.1063/1.3222900.